Available online at www.sciencedirect.com
ScienceDirect
Journal of Nuclear Materials 361 (2007) 94–103
journal of nuclear materials
www.elsevier.com/locate/jnucmat

A close-form solution to predict the total melting time of an ablating slab in contact with a plasma

Feng-Bin Yeh *

Department of Marine Mechanical Engineering, Chinese Naval Academy, P.O. Box 90175, Tsoying, Kaohsiung, Taiwan, ROC

Received 1 August 2006; accepted 27 October 2006

Abstract

An exact melt-through time is derived for a one-dimensional heated slab in contact with a plasma when the melted material is immediately removed. The plasma is composed of a collisionless presheath and sheath on a slab, which partially reflects and secondarily emits ions and electrons. The energy transport from plasma to the surface accounting for the presheath and sheath is determined from the kinetic analysis. This work proposes a semi-analytical model to calculate the total melting time of a slab based on a direct integration of the unsteady heat conduction equation, and provides quantitative results applicable to control the total melting time of the slab. The total melting time as a function of plasma parameters and thermophysical properties of the slab are obtained. The predicted energy transmission factor as a function of dimensionless wall potential agrees well with the experimental data. The effects of reflectivities of the ions and electrons on the wall, electron-to-ion source temperature ratio at the presheath edge, charge number, ion-to-electron mass ratio, ionization energy, plasma flow work-to-heat conduction ratios, Stefan number, melting temperature, Biot number and bias voltage on the total melting time of the slab are quantitatively provided in this work.

1. Introduction

Plasma etching, spray deposition, sputtering, cutting, surface treatment, and nuclear fusion devices, etc., are controlled by energy transfer from the plasma to the workpiece surfaces [1]. There has been intensive theoretical research to study energy and mass transport in the cathode or near wall region of electric arc discharges, lamps, fusion devices, edge plasmas, etc. [2–9]. The surface temperature is strongly influenced by the plasma energy, due to bombardment with energetic particles. Heat transport in the workpiece is determined by the plasma energy transfer, which is controlled by the parameters such as the ion charge number, mass and temperature ratios of the ions and electrons generated in the presheath, and properties of the wall, etc. [10,11]. Yeh and Wei [9] systematically and analytically investigated the plasma energy flux, including ion and electron energy fluxes, and transport to a negatively biased surface in contact with a plasma. Yeh and Wei [10] solved the one-dimensional unsteady conduction equation accounting

---

* Fax: +886 7 5834861.
E-mail address: fbyeh@mail.cna.edu.tw

0022-3115/$ - see front matter © 2006 Elsevier B.V. All rights reserved.
doi:10.1016/j.jnucmat.2006.10.024

for solid–liquid phase change transition with distinct thermal properties in a workpiece using the finite difference method. The effects of plasma characteristics and thermophysical parameters of the workpiece on unsteady temperature profiles and thickness of the molten layer in the workpiece are quantitatively provided. Energy released from the recombination of ions and electrons on the surface is found to play an important role on heating the workpiece. Yeh [11] studied the plasma heating of a film on a substrate by using the Laplace integral transform method to solve the one-dimensional unsteady heat conduction equations for the film and the substrate. An analytical solution is derived to calculate the melting time and heating rate of the front surface of a film on the substrate with negative bias voltage. The effects of plasma parameters on heating rates and melting time for the film are found to be significant.

Plasma facing components (PFCs) in the fusion devices are subject to high quasi-steady state heat loads during normal operation and have to accommodate peak transient energy deposition resulting from off-normal plasma conditions. During a disruption, the intense deposition of energy rapidly increases the surface temperature and causes severe surface erosion and melting of the PFCs dependent on the energy density and deposition time. The exact amount of eroded material and the lifetime of the PFCs are critically important to reactor design. Over the past decades intensive research has been carried out to study the energy transport and predict the lifetime of PFCs used in fusion devices [2,6,12–21]. Raffray and Federici [14,15] developed the transient thermal model RACLETTE, in which evaporation, melting, radiation, and interaction with the PFC block's thermal response and coolant behavior are used to analyse the heat transfer and erosion effects under slow high power energy transients on the actively cooled PFCs. Hassanein and Konkashbaev [16–19] developed a comprehensive numerical model which evaluates the lifetimes of PFCs and predicts various forms of damage such as vaporization, spallation, and liquid splatter of metallic materials. The dependence of the divertor plate lifetime on various aspects of plasma/material interaction physics was analyzed and discussed. However, prediction of the total melting time of an ablating slab in contact with a plasma as functions of plasma parameters and thermophysical properties of the workpieces are still incomplete.

When the incident plasma heat flux is strong enough to cause melting, the problem of one-dimensional unsteady heat conduction in a slab becomes non-linear due to the moving solid–liquid interface, and is therefore more complex. However, it is possible to obtain an exact expression for the time required to totally melt a slab of given thickness for a case in which the melted material is immediately removed. This case is referred to as the ablation case [22]. The aim of the present work is to develop a simple, semi-analytical model to estimate the total melting time for the ablating slab in contact with a plasma. Based on a previously published analysis [9], the slab experiences heating and melting induced by the energy flux from a bulk plasma through the presheath and sheath to the surface. The effects of the plasma parameters and thermophysical properties of the slab on the total melting time are provided.

2. Analytical model

In this study, a slab of finite thickness s at room temperature T_0 is subjected to energy transport from a plasma, as illustrated in Fig. 1. The plasma is comprised of the bulk plasma, presheath and sheath, and is in contact with the front surface of the slab. The front surface can partially reflect or secondarily emit ions and electrons. When a negative bias voltage is applied to the slab, high plasma energy incident on the front surface increases temperatures in the slab and readily results in solid–liquid transition. Heat is removed by convection at the bottom surface of the slab with heat transfer

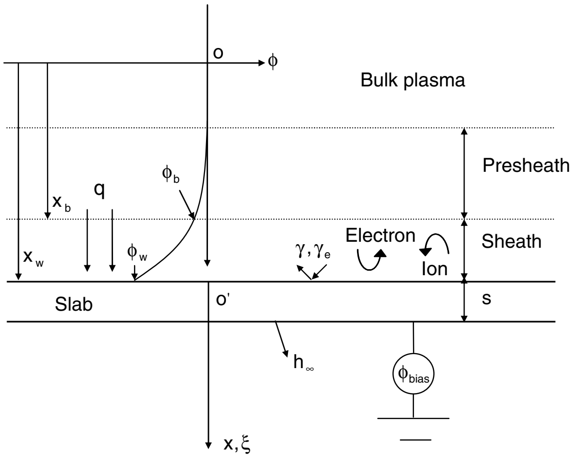

Fig. 1. Sketch of the physical model and coordinates.

coefficient h_∞. Initially, the incident plasma particles from the bulk plasma through the presheath and sheath deposit their energy on the slab surface. At some time $\tau_m > 0$, the surface reaches the melting temperature λ_m, and the melting process begins. Some of various forces such as electromagnetic, plasma particle momentum, etc., may cause melt-layer losses due to the hydrodynamic instabilities [17]. The plasma energy delivered to the slab surfaces will cause sudden ablation of the slab. The front surface of the slab moves toward the bulk and at time $\tau > \tau_m$ its position is given by $\xi = \delta(\tau)$. Taking the solid–liquid phase change, plasma parameters and temperature-independent thermophysical properties of the slab were developed to predict the total melting time of the ablating slab. The major assumptions made are as follows [9–11,23]:

1. The model is one-dimensional due to thin thickness of the region considered.
2. Transport processes in the plasma in contact with the slab surface can be modeled as those in a plasma between two parallel plates.
3. The presheath and sheath are imposed by a negligible magnetic field or a magnetic field in a direction parallel to the ion flow. As a result, the one-dimensional ion flow can be assured.
4. The presheath and sheath are collisionless. The ionization rate is determined from the model by Emmert et al. [24]. This model is based on the fact that the ions would be a Maxwell–Boltzmann distribution in the absence of an electrostatic field far from the wall. This proposition has been confirmed by measurements of the ion distribution functions from Bachet et al. [25], and successful comparisons between the measured ion density and velocity in argon plasma from Goeckner et al. [26] and theoretical prediction by Yeh and Wei [9].
5. The plasma energy flux incident on the front surface of the slab is considered as a surface heat source. Joule heat in the slab and energy loss from thermal radiation are neglected.
6. The plasma is in a quasi-steady state. The incident plasma irradiance on the front surface of the slab is independent of time, while heat transfer in the slab is unsteady.
7. The slab surface is negatively biased electrically.
8. The effects of neutral particles are ignored.
9. Ion and electron reflectivities are constant. The effects of secondary emissions of the ions and electrons can be included into the reflectivities. Thermionic and field emissions of the ions and electrons are ignored.

2.1. Plasma energy transport to workpiece surface

The dimensionless plasma energy flux transport to the workpiece surface subjected to a negative bias voltage is given by [9]:

$$Q = Q_{\mathrm{iw}} + Q_{\mathrm{ew}} + Q_{\mathrm{rec}} + Q_{\mathrm{ab}} = J_{\mathrm{iw}}\left(\Omega + \chi_{\mathrm{w}} - \chi_{\mathrm{b}} + \frac{E_{\mathrm{i}}}{Z_{\mathrm{i}}} - \varphi\right) + J_{\mathrm{ew}}(2+\varphi), \quad (1)$$

where dimensionless energy flux for the ions, electrons, energies for recombination and absorption of the electrons coming from plasma to the workpiece surface are, respectively,

$$Q_{\mathrm{iw}} = J_{\mathrm{iw}}(\Omega + \chi_{\mathrm{w}} - \chi_{\mathrm{b}}), \quad (2)$$

$$Q_{\mathrm{ew}} = 2J_{\mathrm{ew}}, \quad (3)$$

$$Q_{\mathrm{rec}} = J_{\mathrm{iw}}\left(\frac{E_{\mathrm{i}}}{Z_{\mathrm{i}}} - \varphi\right), \quad (4)$$

$$Q_{\mathrm{ab}} = J_{\mathrm{ew}}\varphi. \quad (5)$$

The dimensionless variables and parameters are defined as

$$Q = \frac{q}{n_{\mathrm{e0}}k_{\mathrm{B}}T_{\mathrm{e0}}(k_{\mathrm{B}}T_{\mathrm{e0}}/m_{\mathrm{i}})^{1/2}}, \quad \chi = -\frac{e\phi}{k_{\mathrm{B}}T_{\mathrm{e0}}},$$
$$J = \frac{j}{en_{\mathrm{e0}}(k_{\mathrm{B}}T_{\mathrm{e0}}/m_{\mathrm{i}})^{1/2}}, \quad E_{\mathrm{i}} = \frac{\varepsilon_i}{k_{\mathrm{B}}T_{\mathrm{e0}}}, \quad \varphi = \frac{w_{\mathrm{i}}}{k_{\mathrm{B}}T_{\mathrm{e0}}}, \quad (6)$$

where q and Q, ϕ and χ, j and J, ε_{i} and E_{i}, w_{i} and φ are the dimensional and dimensionless plasma energy flux, potential, current density, ionization energy and work function, respectively. Z_{i} is the ion charge number, k_{B} the Boltzmann constant, e the electron charge, T_{e0} the electron source temperature at the presheath edge, n_{e0} the electron density at the presheath edge and m_{i} the ion mass. The ion and electron current densities at the wall in Eq. (1) are, respectively,

$$J_{\mathrm{iw}} = \Omega_{1\mathrm{b}}e^{-\chi_{\mathrm{b}}}, \quad J_{\mathrm{ew}} = (1-\gamma_{\mathrm{e}})\sqrt{\frac{M}{2\pi}}e^{-\chi_{\mathrm{w}}}, \quad (7)$$

with functions

$$\Omega \equiv \left[\frac{2}{Z_{\mathrm{i}}\kappa} - 1 + \frac{\sqrt{\chi_{\mathrm{b}}}}{D(\sqrt{\chi_{\mathrm{b}}})}\right], \quad (8)$$

$$\Omega_{1\mathrm{b}} \equiv \frac{2(1-\gamma)}{1+\gamma}\sqrt{\frac{2}{Z_{\mathrm{i}}}}\frac{1+Z_{\mathrm{i}}\kappa}{\pi\kappa}e^{\chi_{\mathrm{b}}}D(\sqrt{\chi_{\mathrm{b}}}), \quad (9)$$

where γ and γ_e are the ion and electron reflectivity, respectively, M the ion-to-electron mass ratio defined as $M = m_i/m_e$, κ the electron-to-ion source temperature ratio at the presheath edge defined as $\kappa = T_{e0}/T_{i0}$. Dawson function $D(x)$ is defined in previous study [23]. The sheath edge potential χ_b is satisfied by [23]

$$\frac{2}{\sqrt{\pi Z_i \kappa}} D\left(\sqrt{\chi_b}\right) = e^{Z_i \kappa \chi_b} \operatorname{erfc}\left(\sqrt{Z_i \kappa \chi_b}\right), \tag{10}$$

where function erfc(x) is the complementary error function [23]. The wall potential is equal to the floating potential and the bias voltage for $\chi_{bias} = 0$ and $\chi_{bias} \gg 0$, respectively. The dimensionless wall potential yields [9]

$$\chi_w = \begin{cases} \chi_b + \ln\left(\frac{1-\gamma_e}{\Omega_{1b}}\sqrt{\frac{M}{2\pi}}\right) & \text{for} \quad \chi_{bias} = 0 \\ \chi_{bias} & \text{for} \quad \chi_{bias} \gg 0. \end{cases} \tag{11}$$

Eq. (1) shows that the total energy flux transport to the workpiece surface depends on ion and electron flux, the difference in potentials between the workpiece surface and sheath edge, and recombination energies of the ions and electrons. Since ion and electron densities are equal on the floating wall, i.e., no bias voltage $\chi_{bias} = 0$, the dimensionless plasma energy flux transport to the floating workpiece surface from Eq. (1) can be further expressed as

$$Q = J_{iw}\left(\Omega + \chi_w - \chi_b + \frac{E_i}{Z_i} + 2\right). \tag{12}$$

2.2. Plasma heating of a slab until to initiate melting on the front surface

The one-dimensional, unsteady heat conduction equation for a slab in dimensionless form yields

$$\frac{\partial \lambda(\xi,\tau)}{\partial \tau} = \frac{\partial^2 \lambda(\xi,\tau)}{\partial \xi^2}, \quad 0 \leqslant \xi \leqslant 1, \quad 0 \leqslant \tau \leqslant \tau_m. \tag{13}$$

The initial and boundary conditions of the slab are, respectively,

$$\lambda(\xi,\tau) = 0, \quad \tau = 0, \tag{14}$$

$$-\frac{\partial \lambda(\xi,\tau)}{\partial \xi} = \Theta Q, \quad \xi = 0, \tag{15}$$

$$-\frac{\partial \lambda(\xi,\tau)}{\partial \xi} = Bi\,\lambda(\xi,\tau), \quad \xi = 1. \tag{16}$$

The dimensionless variables and parameters are defined as

$$\lambda = \frac{T - T_\infty}{T_\infty}, \quad \tau = \frac{t}{\left(\rho c_p s^2/k\right)}, \quad \xi = \frac{x}{s},$$
$$\Theta = \frac{n_{e0} k_B T_{e0} (k_B T_{e0}/m_i)^{1/2}}{(k T_\infty / s)}, \quad Bi = \frac{h_\infty s}{k}, \tag{17}$$

where λ is the dimensionless temperature, ξ the dimensionless coordinate, τ the dimensionless time, Θ the ratio between plasma flow work and heat conduction into the slab, Bi the Biot number at the rear surface of the slab, T_∞ the ambient temperature, c_p the specific heat, ρ the density, k the solid thermal conductivity, s the thickness of the slab, t the time, x the Cartesian coordinate and h_∞ the heat transfer coefficient. The critical time, τ_m, is required to initiate melting on the front surface of the slab. Using the Laplace transform method, the solution of Eq. (13) can be expressed as [11]:

$$\lambda(\xi,\tau) = 2\Theta Q \sum_{n=1}^{\infty} \frac{\left(Bi^2 + \beta_n^2\right)\cos \beta_n \xi}{\beta_n^2\left(Bi^2 + Bi + \beta_n^2\right)}\left(1 - e^{-\beta_n^2 \tau}\right). \tag{18}$$

The variables of β_n are eigenvalues satisfied by $\beta_n \tan \beta_n = Bi$.

2.3. Plasma ablating a slab

The one-dimensional, unsteady heat conduction equation in dimensionless form for the slab during the melting process is described by the following equation:

$$\frac{\partial \lambda(\xi,\tau)}{\partial \tau} = \frac{\partial^2 \lambda(\xi,\tau)}{\partial \xi^2}, \quad \delta(\tau) \leqslant \xi \leqslant 1, \quad \tau_m \leqslant \tau. \tag{19}$$

The front boundary condition of the slab is

$$-\frac{\partial \lambda(\xi,\tau)}{\partial \xi} = \Theta Q - \frac{1}{Ste}\frac{d\delta(\tau)}{d\tau},$$
$$\lambda(\xi,\tau) = \lambda_m, \quad \xi = \delta(\tau), \tag{20}$$

where Ste is the Stefan number defined as $Ste = c_p T_\infty / H_f$. H_f is the latent heat of fusion. λ_m is the dimensionless melting temperature, $\delta(\tau)$ is the dimensionless melted thickness, and $\delta(\tau) = 0$ at $\tau = \tau_m$. Eq. (20) expresses the fact that the heat flow into the slab is reduced by heat absorption due to melting. The rear boundary condition of the slab is same as Eq. (16). Eq. (19) is integrated from $\xi = \delta(\tau)$ to $\xi = 1$, by using the boundary conditions given by Eqs. (16) and (20), and the following result is obtained:

$$\Theta Q - \frac{1}{Ste}\frac{\mathrm{d}\delta(\tau)}{\mathrm{d}\tau} - Bi\lambda(1,\tau) = \int_{\delta(\tau)}^{1} \frac{\partial\lambda}{\partial\tau}\mathrm{d}\xi, \tag{21}$$

and the following formula is applied

$$\frac{\partial}{\partial\tau}\int_{\delta(\tau)}^{1}\lambda(\xi,\tau)\mathrm{d}\xi = -\lambda_{\mathrm{m}}\frac{\mathrm{d}\delta(\tau)}{\mathrm{d}\tau} + \int_{\delta(\tau)}^{1}\frac{\partial\lambda(\xi,\tau)}{\partial\tau}\mathrm{d}\xi. \tag{22}$$

After substituting Eq. (22) into Eq. (21), Eq. (21) can be expressed as

$$\begin{aligned}&\Theta Q - \frac{1}{Ste}\frac{\mathrm{d}\delta(\tau)}{\mathrm{d}\tau} - Bi\lambda(1,\tau)\\ &\quad = \lambda_{\mathrm{m}}\frac{\mathrm{d}\delta(\tau)}{\mathrm{d}\tau} + \frac{\partial}{\partial\tau}\int_{\delta(\tau)}^{1}\lambda(\xi,\tau)\mathrm{d}\xi.\end{aligned} \tag{23}$$

At some time $\tau > \tau_{\mathrm{m}}$, the solid is complete melted, i.e., at $\tau = \tau_{\mathrm{f}}$, $\delta(\tau_{\mathrm{f}}) = 1$. τ_{f} is the dimensionless melt-through time of the slab. It is assumed that the temperature at the rear surface of the slab increases linearly with the time during the melting process and $\lambda(1,\tau) = \lambda_{\mathrm{m}}$ at $\tau = \tau_{\mathrm{f}}$. Eq. (23) is integrated from $\tau = \tau_{\mathrm{m}}$ to $\tau = \tau_{\mathrm{f}}$, then

$$\begin{aligned}&\Theta Q(\tau_{\mathrm{f}} - \tau_{\mathrm{m}}) - \left(\lambda_{\mathrm{m}} + \frac{1}{Ste}\right)\\ &\quad - Bi\frac{\lambda_{\mathrm{m}} + \lambda(1,\tau_{\mathrm{m}})}{2}(\tau_{\mathrm{f}} - \tau_{\mathrm{m}})\\ &= \int_{\delta(\tau_{\mathrm{f}})}^{1}\lambda(\xi,\tau_{\mathrm{f}})\mathrm{d}\xi - \int_{\delta(\tau_{\mathrm{m}})}^{1}\lambda(\xi,\tau_{\mathrm{m}})\mathrm{d}\xi.\end{aligned} \tag{24}$$

The first integral on the right-hand side of Eq. (24) vanishes because the limits are equal, $\delta(\tau_{\mathrm{f}}) = 1$. Substituting Eq. (18) at $\tau = \tau_{\mathrm{m}}$ into the second integral on the right-hand side of Eq. (24) and invoking $\delta(\tau_{\mathrm{m}}) = 0$, we get

$$\begin{aligned}\int_{\delta(\tau_{\mathrm{m}})}^{1}\lambda(\xi,\tau_{\mathrm{m}})\mathrm{d}\xi &= 2\Theta Q\sum_{n=1}^{\infty}\frac{(Bi^2+\beta_n^2)\sin\beta_n}{\beta_{\mathrm{n}}^3(Bi^2+Bi+\beta_n^2)}\\ &\qquad \times\left(1 - e^{-\beta_{\mathrm{n}}^2\tau_{\mathrm{m}}}\right).\end{aligned} \tag{25}$$

Substituting $\xi = 1$ into Eq. (18), the temperature at the rear surface of the slab at $\tau = \tau_{\mathrm{m}}$ is

$$\begin{aligned}\lambda(1,\tau_{\mathrm{m}}) &= 2\Theta Q\sum_{n=1}^{\infty}\frac{(Bi^2+\beta_{\mathrm{n}}^2)\cos\beta_{\mathrm{n}}}{\beta_{\mathrm{n}}^2(Bi^2+Bi+\beta_n^2)}\\ &\qquad \times\left(1 - e^{-\beta_{\mathrm{n}}^2\tau_{\mathrm{m}}}\right).\end{aligned} \tag{26}$$

After substituting Eqs. (25) and (26) into Eq. (24), the dimensionless total melting time is expressed as

$$\tau_{\mathrm{f}} = \tau_{\mathrm{m}} + \frac{\lambda_{\mathrm{m}} + \frac{1}{Ste} - 2\Theta Q\sum\limits_{\mathrm{n}=1}^{\infty}\frac{(Bi^2+\beta_{\mathrm{n}}^2)\sin\beta_{\mathrm{n}}}{\beta_{\mathrm{n}}^3(Bi^2+Bi+\beta_{\mathrm{n}}^2)}\times\left(1 - e^{-\beta_{\mathrm{n}}^2\tau_{\mathrm{m}}}\right)}{\Theta Q - \frac{Bi}{2}\left[\lambda_{\mathrm{m}} + 2\Theta Q\sum\limits_{\mathrm{n}=1}^{\infty}\frac{(Bi^2+\beta_n^2)\cos\beta_n}{\beta_{\mathrm{n}}^2(Bi^2+Bi+\beta_{\mathrm{n}}^2)}\times\left(1 - e^{-\beta_{\mathrm{n}}^2\tau_{\mathrm{m}}}\right)\right]}. \tag{27}$$

Substituting $\xi = 0$ into Eq. (18), the temperature at the front surface of the slab at $\tau = \tau_{\mathrm{m}}$ is

$$\begin{aligned}\lambda(0,\tau_{\mathrm{m}}) &= 2\Theta Q\sum_{\mathrm{n}=1}^{\infty}\frac{Bi^2+\beta_{\mathrm{n}}^2}{\beta_{\mathrm{n}}^2(Bi^2+Bi+\beta_{\mathrm{n}}^2)}\\ &\qquad \times\left(1 - e^{-\beta_{\mathrm{n}}^2\tau_{\mathrm{m}}}\right).\end{aligned} \tag{28}$$

The critical time, τ_{m}, can be determined by bisection method from Eq. (28) when $\lambda(0,\tau_{\mathrm{m}})$ is equal to λ_{m}.

3. Results and discussion

To confirm relevancy and accuracy of this model, the predicted energy transmission factor between a helium plasma and tungsten workpiece as a function of dimensionless wall potential is compared with experimental data provided by Masuzaki et al. [12], as shown in Fig. 2. The energy transmission factor η is defined as [2]:

$$\eta = \frac{q}{k_{\mathrm{B}}T_{\mathrm{e}}n_{\mathrm{ib}}\left(\frac{k_{\mathrm{B}}T_{\mathrm{e}}}{m_{\mathrm{i}}} + \frac{k_{\mathrm{B}}T_{\mathrm{i}}}{m_{\mathrm{i}}}\right)^{1/2}} = \frac{Q}{n_{\mathrm{ib}}^*}\left(1 + \frac{1}{\kappa}\right)^{-1/2}, \tag{29}$$

where the dimensionless ion density at the sheath edge is defined as $n_{\mathrm{ib}}^* = n_{\mathrm{ib}}/n_{\mathrm{e0}}$. The electron temperature at the sheath edge is considered to be identical to that at the presheath edge, while the ion temperature at the sheath edge is the ion source temperature at the presheath edge. Choosing dimensionless parameters $\gamma = 0.5$, $\gamma_{\mathrm{e}} = 0$, $\kappa = 10$, $Z_{\mathrm{i}} = 1$, $M = 7344$, $E_{\mathrm{i}} = 14.3$, $\varphi = 2.5$, the predicted energy transmission factor as a function of wall potential agrees

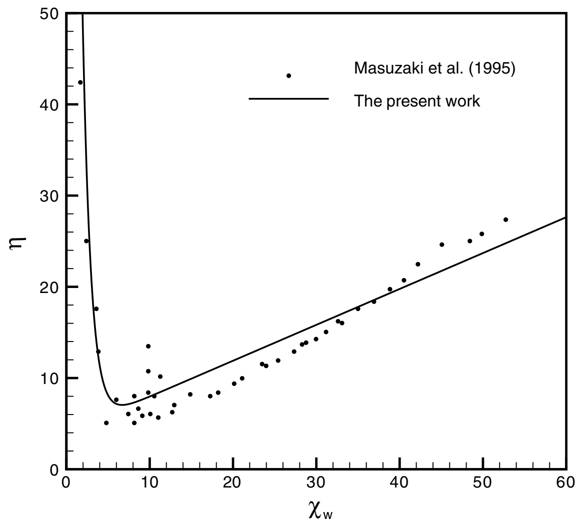

Fig. 2. A comparison between the measurements [12] and predicted energy transmission factor as a function of dimensionless wall potential.

quite well with experimental data [12]. The deviation can be due to the unavailable ion and electron temperatures at the sheath edge.

Figs. 3–8 show the effects of plasma parameters, including reflectivities of ions and electrons (γ, γ_e), electron-to-ion source temperature ratio at the presheath edge (κ), charge number (Z_i), ion-to-electron mass ratio (M) and dimensionless ionization energy (E_i) on the dimensionless energy flux, melting time at the front surface and total melting time of the slab, respectively. The lines (and following figures) are the predicted results based on the reference dimensionless parameters from Table 1, which are estimated from the data for a hydrogen plasma and tungsten workpiece with floating voltage, $\phi_{\text{bias}} = 0$, as listed in Table 2. Even though the dimensionless wall potential is increased with ion reflectivity, decreases in ion and electron currents [9,23] reduce total plasma energy transport to the slab. An increase in ion reflectivity from $\gamma = 0$ to 0.9 results in a decrease in energy flux from $Q = 60.6\,(q \approx 21.5\ \text{GJ/m}^2)$ to $3.58\,(q \approx 1.3\ \text{GJ/m}^2)$, and increases in the melting time from $\tau_m = 3.4 \times 10^{-4}$

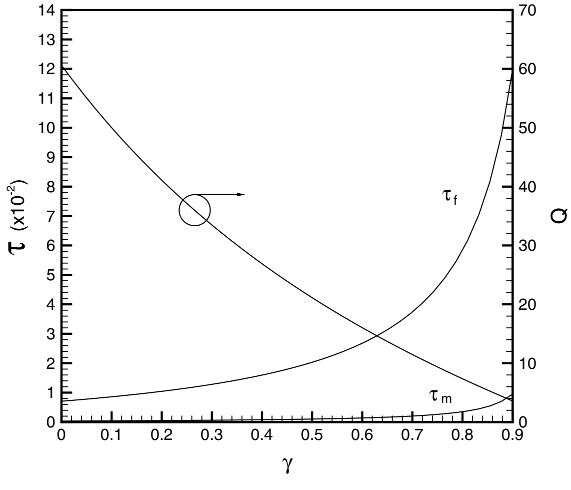

Fig. 3. Dimensionless energy flux, melting times at the front surface and total melting times of a slab affected by the ion reflectivity.

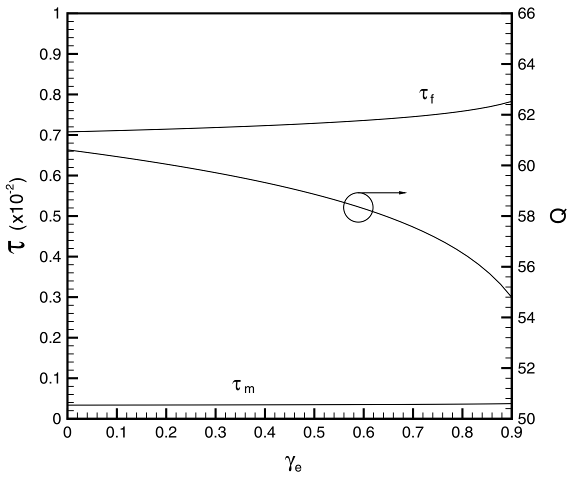

Fig. 4. Dimensionless energy flux, melting times at the front surface and total melting times of a slab affected by the electron reflectivity.

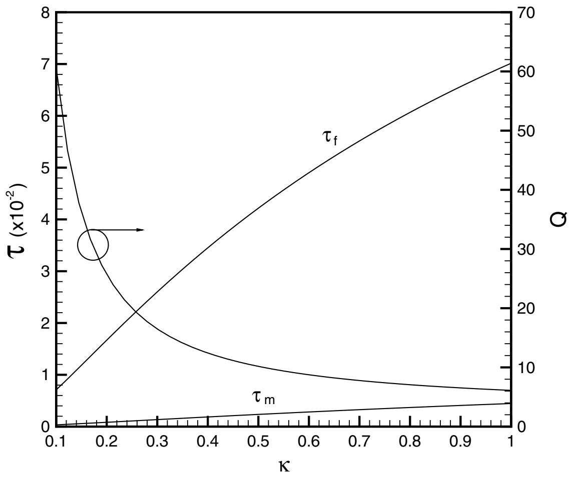

Fig. 5. Dimensionless energy flux, melting times at the front surface and total melting times of a slab affected by the electron-to-ion source temperature ratio at the presheath edge.

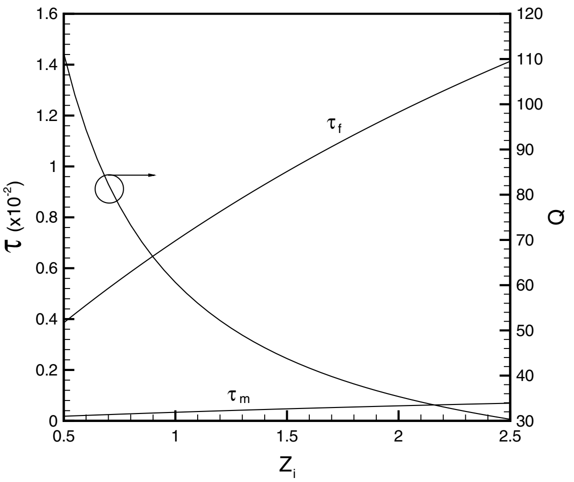

Fig. 6. Dimensionless energy flux, melting times at the front surface and total melting times of a slab affected by the charge number.

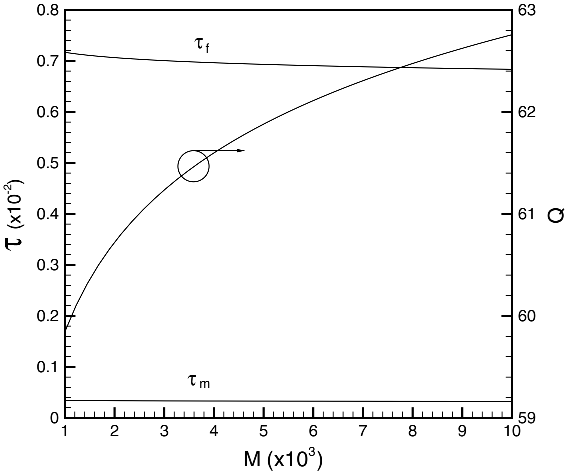

Fig. 7. Dimensionless energy flux, melting times at the front surface and total melting times of a slab affected by the ion-to-electron mass ratio.

($t \approx 0.146$ ms) to 9.5×10^{-3} ($t \approx 4.1$ ms) and the total melting time from $\tau_f = 7.1 \times 10^{-3}$ ($t \approx 3$ ms) to 0.12 ($t \approx 52$ ms). The melting time and total melting time for $\gamma = 0.9$ are 28 times and 17 times larger than those for $\gamma = 0$, respectively. The melting and total melting times rapidly rise with increasing the ion reflectivity as shown in Fig. 3.

On the other hand, an increase in the electron reflectivity decreases the dimensionless wall potential [9,23]. Since ion and electron currents are independent of electron reflectivity [9,23], an increase in electron reflectivity reduces energy transport to the surface. Compared to the ion reflectivity, the effects of increasing the electron reflectivity on the energy flux, melting and total melting times are small. By

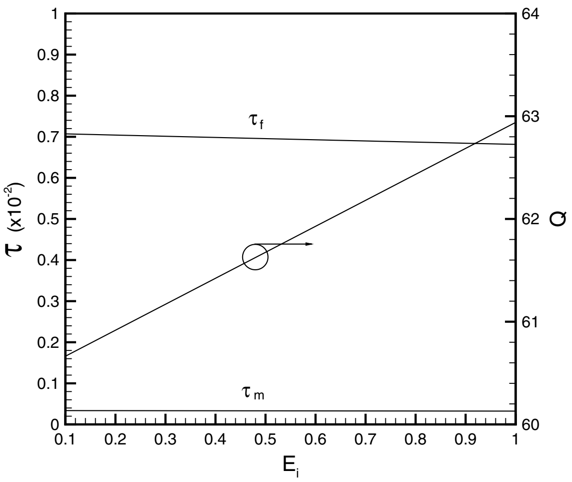

Fig. 8. Dimensionless energy flux, melting times at the front surface and total melting times of a slab affected by the dimensionless ionization energy.

Table 1
Values of the reference dimensionless parameters

γ	0
γ_e	0
κ	0.1
Z_i	1
M	1836
E_i	0.08
Θ	38
Ste	0.2
λ_m	11.3
Bi	3×10^{-3}
χ_{bias}	0

Table 2
Values of the data (hydrogen plasma and tungsten workpiece) used for estimating the reference dimensionless parameters

H_f	2.2×10^5 J/kg
c_p	138 J/kg K
T_0, T_∞	300 K
T_m	3683 K
k	155 W/m K
ρ	19350 kg/m^3
s	0.005 m
h_∞	100 W/m^2 K
n_{e0}	1×10^{20} m^{-3}
m_i	1.67×10^{-27} kg
T_{e0}	2×10^6 K
ε_i	13.6 eV
w_i	4.55 eV

increasing the electron reflectivity from $\gamma_e = 0$ to 0.9, the melting time increases from $\tau_m = 3.4 \times 10^{-4}$ to 3.74×10^{-4} and the total melting time increases from $\tau_f = 7.1 \times 10^{-3}$ to 7.8×10^{-3} as shown in Fig. 4. Fig. 5 shows that as the electron-to-ion source temperature ratio at the presheath edge increases from $\kappa = 0.1$ to 1, the energy flux rapidly drop from $Q = 60.6$ to 6.1, the total melting time increases from $\tau_f = 7.1 \times 10^{-3}$ to 0.07. The energy flux for $\kappa = 0.1$ is around 9.9 times larger than those for $\kappa = 1$. The total melting time of the latter is around 9.9 times larger than those of the former. A high electron-to-ion source temperature ratio indicates that generation of ions is low. To balance electron current, a high dimensionless wall potential is required and results in reduction of electron current (and ion current) [9,23]. Energy transport to the surface is therefore decreased. Fig. 6 shows that as the ion charge number increases from $Z_i = 0.5$ to 2.5, the total melting time increases from $\tau_f = 3.85 \times 10^{-3}$ to 0.014. An increase in charge number decreases the ion energy and increases the electron energy transport to the slab [9]. However, the plasma energy transport to the slab decreases with increasing the charge number in this considered range.

As in the case of the electron reflectivity, the effects of increasing the ion-to-electron mass ratio (M) on the melting and total melting times are small, as shown in Fig. 7. It can be seen that an increase in ion-to-electron mass ratio results in decreasing the dimensionless melting and total melting times. This is because an increase in ion-to-electron mass ratio increases the dimensionless wall potential [9,23], which enhances ion energy or total energy transport from the plasma to the slab. In this case, the ion and electron currents are constants and independent of the ion-to-electron mass ratio. Recombination energy is the difference between the ionization energy and work function. The dimensionless ionization energy of $E_i = 0.08$ corresponds to dimensional ionization energy of $\varepsilon_i = 13.6$ eV for hydrogen plasma (see Tables 1 and 2). In view of a significant energy release from recombination of the ions and electrons on the surface for low plasma energy flux [10], the recombination energy compared to the incident energy of plasma is small for high plasma energy fluxes in this study. An increase in dimensionless ionization energy from $E_i = 0.1$ ($\varepsilon_i = 17.2$ eV) to 1 ($\varepsilon_i = 172$ eV) results in increasing slightly the plasma energy flux ($Q = 60.67$–62.94). The dimensionless melting time and total melting time of the slab are decreased with increasing the dimensionless ionization energy, as shown in Fig. 8. The results show that the effects of plasma parameters such as ion and electron reflectivities, electron-to-ion source temperature ratio and charge number on the melting and total melting times of the slab are significant.

The effects of independent dimensionless parameters governing thermophysical properties of the slab on dimensionless melting time and total melting time of the slab are shown in Figs. 9–11, respectively. It is found that the dimensionless melting and total melting times are decreased with increasing the plasma flow work-to-heat conduction ratio (Θ), as shown in Fig. 9. This is attributed to an increase in internal energy required to raise temperature. As the plasma flow work-to-thermal conduction ratio reduces to one-tenth (from $\Theta = 100$ to 10), the total melting time increases around 10 folds. Increasing the Stefan number indicates a decrease in latent heat for melting. The heat flux required to melt the front of the solid is reduced and the melting front of the solid moves quickly toward the bulk. The total melting time decreases (from $\tau_f = 9.25 \times 10^{-3}$ to 5.34×10^{-3}) with increasing the Stefan number (from $Ste = 0.1$ to 1), but the melting time is not affected ($\tau_m = 3.4 \times 10^{-4}$), as shown in Fig. 10. An increase in the dimensionless melting temperature (λ_m), however, delays the melting time of the front

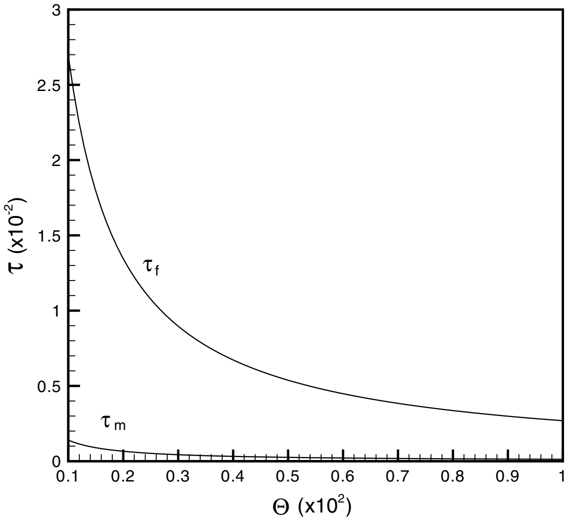

Fig. 9. Dimensionless melting times at the front surface and total melting times of a slab affected by the plasma flow work-to-thermal conduction ratio.

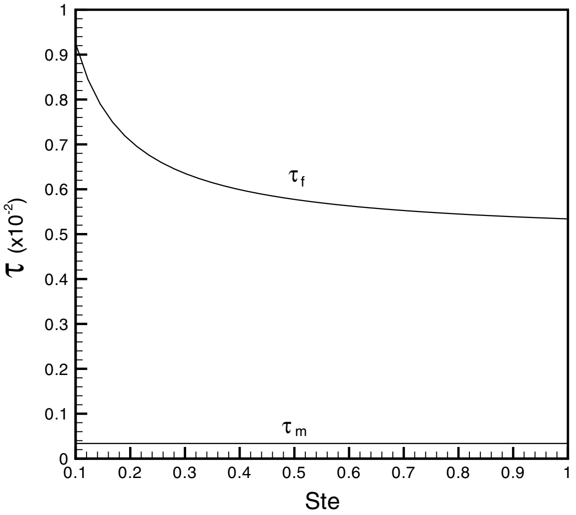

Fig. 10. Dimensionless melting times at the front surface and total melting times of a slab affected by the Stefan number.

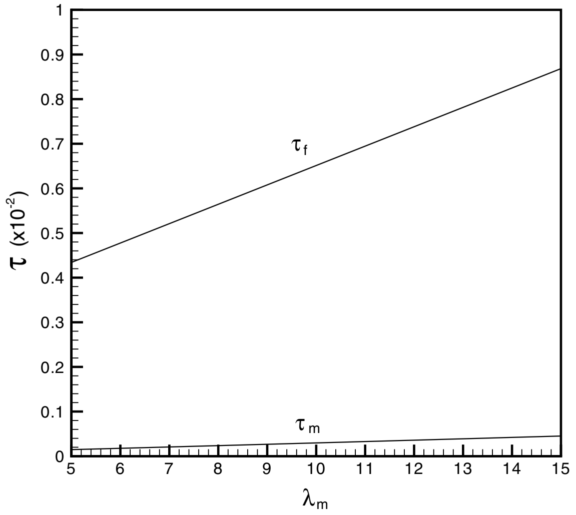

Fig. 11. Dimensionless melting times at the front surface and total melting times of a slab affected by the dimensionless melting temperature.

surface of the slab. Fig. 11 presents the dimensionless melting time and the total melting time of the slab as a function of the dimensionless melting temperature. The higher the melting temperature, the more heat flux is required to melt the slab. Hence, the melting and total melting times increase with the melting temperature. An increase in the melting temperature from $\lambda_m = 5$ ($T_m \approx 1800$ K) to 15 ($T_m \approx 4800$ K) results in increases in the melting time from $\tau_m = 1.47 \times 10^{-4}$ ($t \approx 0.06$ ms) to 4.52×10^{-4} ($t \approx 0.194$ ms) and the total melting time from $\tau_f = 4.34 \times 10^{-3}$ ($t \approx 1.87$ ms) to 8.68×10^{-3} ($t \approx 3.73$ ms). The melting time and total melting time for $\lambda_m = 15$ are around 3 times and 2 times larger than those for $\lambda_m = 5$, respectively.

The higher the Biot number, the quicker the heat is removed by convection to the surroundings. The melting and total melting times increase with the Biot number as shown in Fig. 12. It can be seen that the Biot number increases 10 folds ($Bi = 10$–100), the total melting time increases 1.3 folds (from

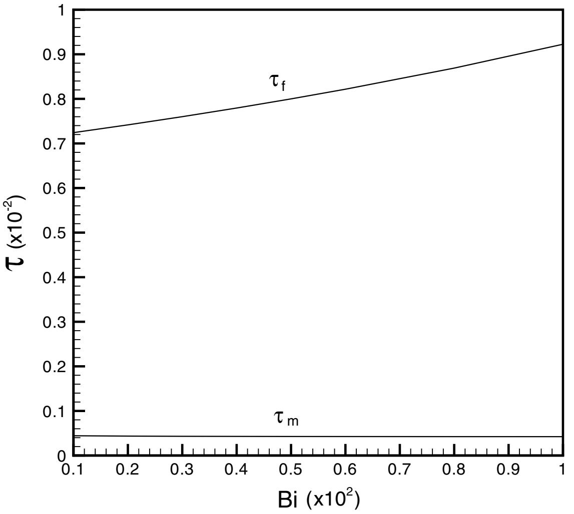

Fig. 12. Dimensionless melting times at the front surface and total melting times of a slab affected by the Biot number.

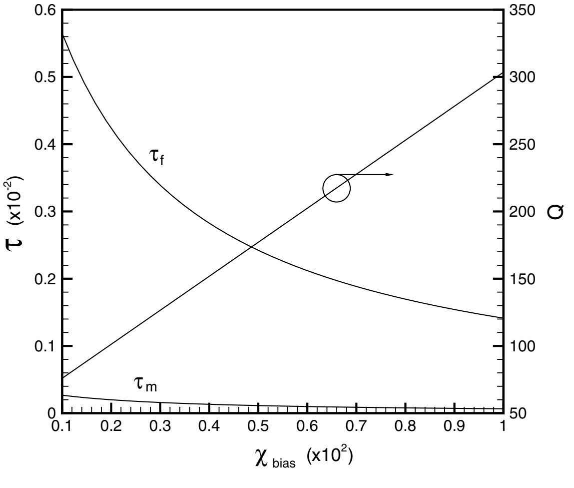

Fig. 13. Dimensionless energy flux, melting times at the front surface and total melting times of a slab for $\varphi = 0.026$ affected by the dimensionless bias voltage.

$\tau_f = 7.24 \times 10^{-3}$ to 9.23×10^{-3}). When a high negative bias voltage is applied to the slab, the potential drop between the slab surface and the sheath edge is increased and the ions gain kinetic energy from the sheath is large. The larger the dimensionless bias voltage, the more the plasma energy transport to the surface. An increase in the dimensionless bias voltage from $\chi_{\text{bias}} = 10\,(\phi_{\text{bias}} \approx -1.7\,\text{kV})$ to 100 ($\phi_{\text{bias}} \approx -17\,\text{kV}$) results in an increase in energy flux from $Q = 76\,(q \approx 27\,\text{GJ/m}^2)$ to $303\,(q \approx 108\,\text{GJ/m}^2)$ and a decrease in the total melting time from $\tau_f = 5.65 \times 10^{-3}\,(t \approx 2.43\,\text{ms})$ to $1.41 \times 10^{-3}\,(t \approx 0.61\,\text{ms})$, as shown in Fig. 13.

4. Conclusions

1. Prediction of the melting and total melting times of the workpiece due to intense energy deposition on the workpiece surface are important for high-energy physics application; thermonuclear and inertial fusion studies, etc. A simple semi-analytical solution is derived to calculate the total melting time of an ablating slab in contact with a plasma when the melted material is immediately removed. The total melting time as a function of plasma parameters and thermophysical properties of the slab are obtained. The predicted energy transmission factor as a function of dimensionless wall potential agrees well with the experimental data. The effects of plasma parameters and thermophysical properties of the slab on the total melting time of the slab are found to be significant. The results can be used to predict the total melting time of the slab by choosing appropriate process parameters to avoid a melt-through of the plasma facing components in the fusion devices. The results should be also useful in several heat transfer applications for high-energy physics application.
2. The total melting time of the slab increases with decreasing ion-to-electron mass ratio, ionization energy, plasma flow work-to-heat conduction ratio, Stefan number and bias voltage, and increasing reflectivities of ions and electrons, electron-to-ion source temperature ratio at the presheath edge, charge number, melting temperature and Biot number. The dimensionless parameters are reversed to decrease the total melting time.

References

[1] H. Kersten, H. Deutsch, H. Steffen, G.M.W. Kroesen, R. Hippler, Vacuum 63 (2001) 385.
[2] P.C. Stangeby, Phys. Fluids 27 (1984) 682.
[3] M.S. Benilov, A. Marotta, J. Phys. D: Appl. Phys. 28 (1995) 1869.
[4] K.C. Hsu, E. Pfender, J. Appl. Phys. 54 (1983) 3818.
[5] H. Schmitz, K.-U. Riemann, J. Phys. D: Appl. Phys. 35 (2002) 1727.
[6] S. Takamura, M.Y. Ye, T. Kuwabara, N. Ohno, Phys. Plasmas 5 (1998) 2151.
[7] D. Uhrlandt, D. Loffhagen, S. Arndt, R. Winkler, Surf. Coat. Technol. 142–144 (2001) 517.
[8] P.C. Stangeby, J. Phys. D: Appl. Phys. 15 (1982) 1007.
[9] F.B. Yeh, P.S. Wei, Int. J. Heat Mass Transfer 47 (2004) 4019.
[10] F.B. Yeh, P.S. Wei, ASME J. Heat Transfer 127 (2005) 987.
[11] F.B. Yeh, Int. J. Heat Mass Transfer 49 (2006) 297.
[12] S. Masuzaki, N. Ohno, S. Takamura, J. Nucl. Mater. 223 (1995) 286.
[13] M. Araki, M. Kobayashi, Rev. Sci. Instrum. 67 (1996) 178.
[14] A.R. Raffray, G. Federici, J. Nucl. Mater. 244 (1997) 85.
[15] G. Federici, A.R. Raffray, J. Nucl. Mater. 244 (1997) 101.
[16] A. Hassanein, I. Konkashbaev, Fusion Eng. Des. 28 (1995) 27.
[17] A. Hassanein, I. Konkashbaev, J. Nucl. Mater. 233–237 (1996) 713.
[18] A. Hassanein, I. Konkashbaev, Fusion Eng. Des. 51&52 (2000) 681.
[19] A. Hassanein, Fusion Eng. Des. 60 (2002) 527.
[20] V.N. Litunovsky, A.A. Drozdov, V.E. Kuznetsov, I.B. Ovchinnikov, V.A. Titov, Fusion Eng. Des. 39&40 (1998) 303.
[21] I. Šmid, H.D. Pacher, G. Vieider, U. Mszanowski, Y. Igitkhanov, G. Janeschitz, J. Schlosser, L. Plöchl, J. Nucl. Mater. 233–237 (1996) 701.
[22] J.E. Rogerson, G.A. Chayt, J. Appl. Phys. 42 (1971) 2711.
[23] P.S. Wei, F.B. Yeh, IEEE Trans. Plasma Sci. 28 (2000) 1233.
[24] G.A. Emmert, R.M. Wieland, A.T. Mense, J.N. Davidson, Phys. Fluids 23 (1980) 803.
[25] G. Bachet, L. Cherigier, F. Doveil, Phys. Plasmas 2 (1995) 1782.
[26] M.J. Goeckner, J. Goree, T.E. Sheridan, Phys. Fluids B 4 (1992) 1663.